Development of the human fetal immune system: novel insights from high-dimensional single-cell technologies

Li, N.


JEM
Journal of Experimental Medicine
VOL 215 • NO 5 • MAY 2018
WWW.JEM.ORG
Rockefeller University Press

Chapter 2

Mass Cytometry Reveals Innate Lymphoid Cell Differentiation Pathways in the Human Fetal Intestine

Na Li,[1,*] Vincent van Unen,[1,*] Thomas Höllt,[2,3] Allan Thompson,[1] Jeroen van Bergen,[1] Nicola Pezzotti,[2] Elmar Eisemann,[2] Anna Vilanova,[2] Susana M. Chuva de Sousa Lopes,[4] Boudewijn P.F. Lelieveldt,[5,6] Frits Koning[1]

[1] Department of Immunohematology and Blood Transfusion, Leiden University Medical Center, Leiden, Netherlands

[2]Computer Graphics and Visualization Group, Delft University of Technology, Delft, Netherlands

[3]Computational Biology Center, Leiden University Medical Center, Leiden, Netherlands

[4]Department of Anatomy and Embryology, Leiden University Medical Center, Leiden, Netherlands

[5]Department of LKEB Radiology, Leiden University Medical Center, Leiden, Netherlands

[6] Department of Pattern Recognition and Bioinformatics group, Delft University of Technology, Delft, Netherlands

* Equal contribution

Journal of Experimental Medicine 215:5, 1383-1396 (2018)

ON THE COVER

Li et al. apply mass cytometry to delineate the fetal gut innate lymphoid cell (ILC) population and use a t-SNE-based approach to predict potential differentiation trajectories. This image represents the composition of the ILC compartment in the individual fetal intestines. The image was taken from the original manuscript and modified by the *JEM* editorial office. See page 77

Abstract

Innate lymphoid cells (ILCs) are abundant in mucosal tissues and involved in tissue homeostasis and barrier function. While several ILC subsets have been identified, it is unknown if additional heterogeneity exists and their differentiation pathways remain largely unclear. We applied mass cytometry to analyze ILCs in the human fetal intestine and distinguished 34 distinct clusters through a t-SNE-based analysis. A lineage (Lin)$^-$CD7$^+$CD127$^-$CD45RO$^+$CD56$^+$ population clustered between the CD127$^+$ ILC and natural killer (NK) cell subsets, and expressed diverse levels of Eomes, T-bet, GATA3 and RORγt. By visualizing the dynamics of the t-SNE computation, we identified smooth phenotypic transitions from cells within the Lin$^-$CD7$^+$CD127$^-$CD45RO$^+$CD56$^+$ cluster to both the NK cells and CD127$^+$ ILCs, revealing potential differentiation trajectories. In functional differentiation assays the Lin$^-$CD7$^+$CD127$^-$CD45RO$^+$CD56$^+$CD8a$^-$ cells could develop into CD45RA$^+$ NK cells and CD127$^+$RORγt$^+$ ILC3-like cells. Thus, we identified a previously unknown intermediate innate subset that can differentiate into ILC3 and NK cells.

Introduction

Innate lymphoid cells (ILCs) lack expression of T cell receptors but otherwise are a functional counterpart of cytotoxic and helper T cell subsets. Helper ILCs are classified into 3 groups: ILC1, ILC2 and ILC3 [1]. ILC1s are mainly characterized as Lineage (Lin)$^-$CD161$^+$CD127$^+$CRTH2$^-$CD117$^-$, express the transcription factor T-bet and produce T helper 1 (T_H1) cell-associated cytokines. ILC2s are Lin$^-$CD161$^+$CD127$^+$CRTH2$^+$, express GATA3, and produce T helper 2 (T_H2) cell-associated cytokines. ILC3s, including fetal lymphoid tissue-inducer (LTi) cells, are Lin$^-$CD161$^+$CD127$^+$CRTH2$^-$CD117$^+$, RORγt$^+$, and secrete T_H17/T_H22 helper T cell-associated cytokines [1,2]. A fraction of human ILC3s expresses natural cytotoxicity receptors such as NKp44, NKp46 and NKp30, and neural cell adhesion molecule CD56, similar to natural killer (NK) cells [3,4]. NK cells are a cytotoxic subset of ILCs that express the transcription factor T-bet and/or Eomes and produce IFN-γ, granzymes and perforin [1]. Also, ILCs are most abundant and reside in (mucosal) tissues such as the tonsil, lung and intestine, where they can expand locally [5].

Several studies have reported the differentiation pathways of ILCs in a variety of tissues in both mice and humans [6,7]. For example, in murine fetal liver and adult intestine, a CXCR6$^+$RORγt$^+$α4β7$^+$ subset has been identified that can differentiate into ILC3s and NK cells [8]. As this subset was not found in adult bone marrow, it might migrate to the intestine during fetal development. In humans, RORγt$^+$CD34$^+$ progenitor cells were identified in the tonsil and intestine, but these were absent in peripheral blood, umbilical cord blood, bone marrow and thymus [9,10]. Since these progenitors could differentiate into helper ILCs and NK cells, mucosal organs might be the preferential sites for ILC differentiation. In addition, a CD127$^+$CD117$^+$ ILC precursor (ILCP) has been identified in cord blood, peripheral blood and tissues, including fetal liver, adult lung and tonsil, which can generate all ILC subsets in situ and could represent an intermediate between precursor cells and mature ILCs [11]. Also, previous studies have observed ILC plasticity mainly in mucosal tissues, such as the small intestine [12–15], suggesting that environmental cues may play an important role in cell-fate decision. So far, most of the studies on human ILC differentiation used CD34$^+$ progenitors and mature types of ILCs [6], while the intermediates or transitional stages connecting the CD34$^+$ populations to mature types of ILCs have not been fully identified.

High-dimensional mass cytometry provides an opportunity to analyze the heterogeneity and potential differentiation pathways of human ILCs in an unbiased and data-driven fashion based on the simultaneous measurement of over 30 cellular markers at single-cell resolution [16]. Although the sensitivity of

metal reporters in mass cytometry is not as sensitive as some of the brightest fluorochromes in flow cytometry, the advantage of including many more markers in a single antibody panel offers unique opportunities to evaluate the composition of the immune system with unprecedented resolution. Up to recently, analysis of flow cytometry data was mainly performed with gating strategies based on (primarily) bimodal expression patterns. The incorporation of over 30 markers in mass cytometry antibody panels is not well compatible with such an analysis approach. Instead, t-Distributed Stochastic Neighbor Embedding (t-SNE)-based approaches are currently becoming the standard in the field as they allow the simultaneous analysis of all marker expression profiles in an unbiased fashion. Hierarchical SNE, for example, allows efficient analysis of mass cytometry data sets on tens of millions of cells at the single-cell level [17]. Here, we applied mass cytometry to analyze the ILC compartment in the human fetal intestine and provide evidence for previously unrecognized heterogeneity within this compartment. Moreover, we utilized a t-SNE-based computational approach to predict potential differentiation trajectories in silico, and provide evidence for the existence of a previously unrecognized innate cell subset that can differentiate into both NK cells and ILC3 in vitro.

Results

High-dimensional analysis reveals previously unrecognized heterogeneity in the ILC compartment

We developed a 35 metal isotope-tagged monoclonal antibody panel (**Table S1**) to identify the 6 major immune lineages (B cells, myeloid cells, $CD4^+$, $CD8^+$, γδ T cells, and Lin^-CD7^+ cells; the latter hereafter referred to as ILCs) and heterogeneity within those lineages. For this purpose the panel included lineage markers and markers linked to cell differentiation, activation, trafficking and responsiveness to humoral factors. With this panel, single-cell suspensions prepared from 7 fetal intestines were analyzed individually. Single, live $CD45^+$ cells were discriminated by event length, DNA stainings and CD45 antibody staining (**Fig. S1 A**). All antibodies showed clear discrimination between antibody-positive and -negative cells (**Fig. S1 B**). Similar to our previous study [18], we applied a combined t-SNE [19]-ACCENSE [20] data analysis approach to the 6 major cell lineages (**Fig. S1 C**) which revealed a large degree of heterogeneity within these lineages.

We next focused on the ILC compartment (**Fig. S2 A**) which comprised 20.4% ± 7.8% of the $CD45^+$ cells. We pooled the data from the 7 samples and performed a

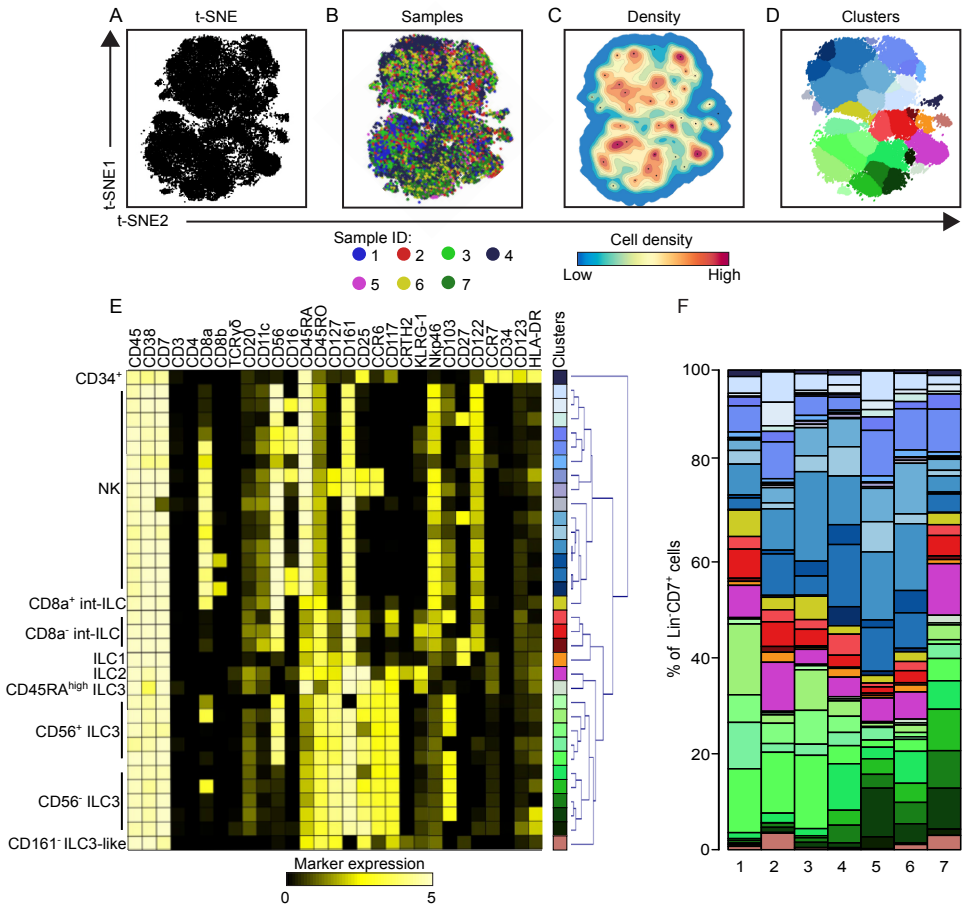

Fig. 1. High-dimensional mass cytometry analysis reveals previously unrecognized heterogeneity in the fetal intestinal ILC compartment (**A**) A t-SNE embedding showing the collective ILCs ($4.5x10^4$ cells) derived from 7 fetal intestines, each black dot represents a single cell. (**B**) A t-SNE embedding as shown in panel A. Colors represent the different samples. (**C**) A density map describing the local probability density of t-SNE-embedded cells where black dots represent centroids of identified clusters using Gaussian Mean Shift clustering. (**D**) A t-SNE plot showing cluster partitions in different colors. (**E**) Heatmap showing the median ArcSinh5-transformed marker expression values (black-to-yellow scale) of the clusters identified in panel A with description of ten annotated categories based on pre-existing literature, and hierarchical clustering thereof. (**F**) Composition of the ILC compartment in the individual fetal intestines (N=7) represented in vertical bars where the size of the colored segments represents the proportion of cells as % of total ILC in the sample. Colors as in panel A.

t-SNE analysis in Cytosplore [21]. This provided a two-dimensional map where cellsare positioned based on the similarity in expression of all marker simultaneously (**Fig. 1 A and B**). Based on the density features of the t-SNE-embedded cells, we identified 34 phenotypically distinct clusters (**Fig. 1, C and D**) using the Gaussian Mean Shift clustering and generated a heatmap showing the distinct marker

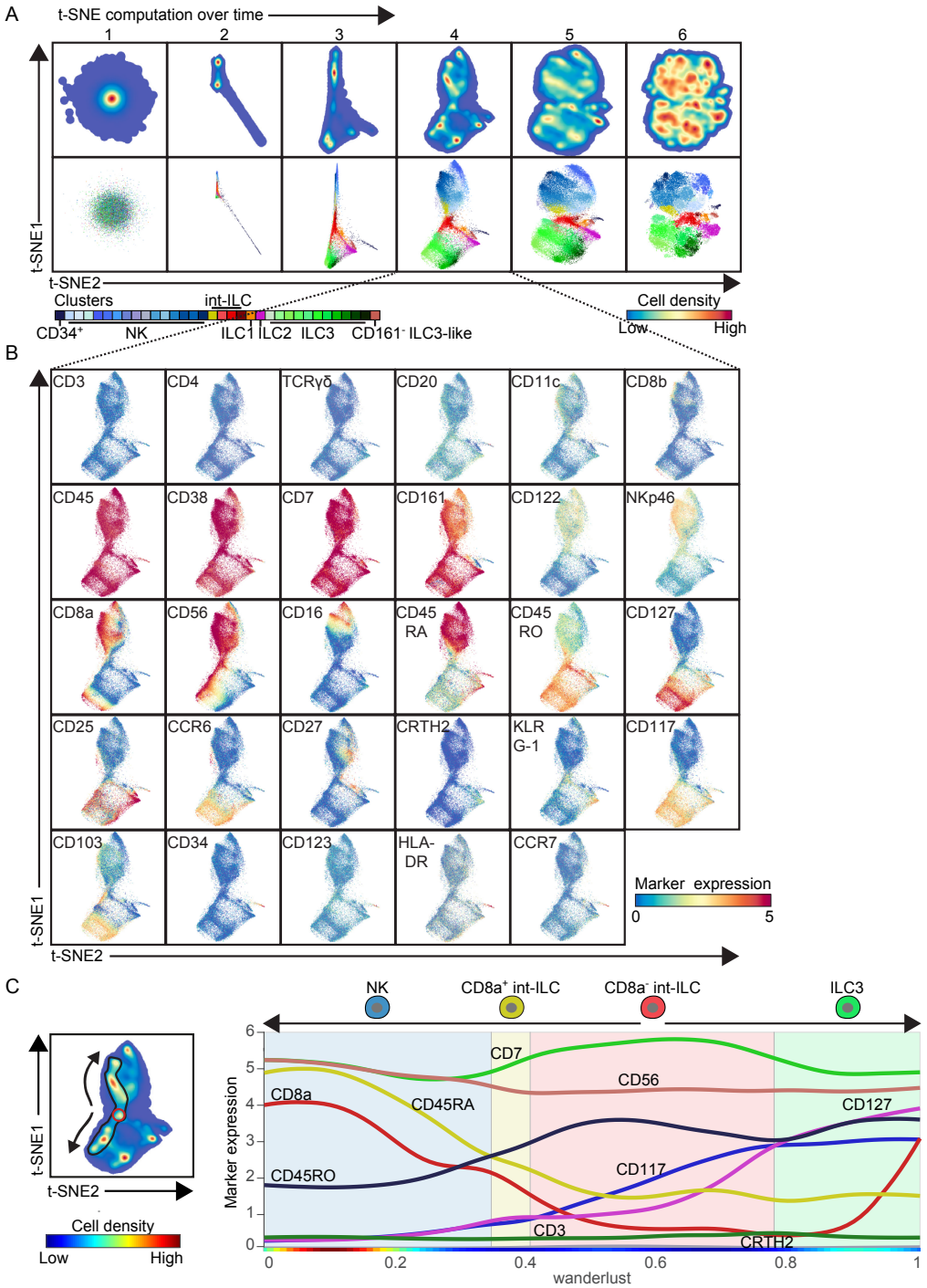
A
t-SNE computation over time
1
2
3
4
5
6
t-SNE1
t-SNE2
Clusters
int-ILC
Cell density
CD34+
NK
ILC1
ILC2
ILC3
CD161- ILC3-like
Low
High
B
CD3
CD4
TCRγδ
CD20
CD11c
CD8b
CD45
CD38
CD7
CD161
CD122
NKp46
CD8a
CD56
CD16
CD45 RA
CD45 RO
CD127
CD25
CCR6
CD27
CRTH2
KLR G-1
CD117
CD103
CD34
CD123
HLA-DR
CCR7
Marker expression
0
5
t-SNE1
t-SNE2
C
NK
CD8a+ int-ILC
CD8a- int-ILC
ILC3
t-SNE1
t-SNE2
Cell density
Low
High
Marker expression
CD8a
CD45RA
CD7
CD56
CD127
CD45RO
CD117
CD3
CRTH2
wanderlust

expression profiles for each cluster (**Fig. 1 E**). Unbiased hierarchical clustering revealed distinct clusters including a group of $CD34^+$ cells expressing CD45RA and CD117, a larger cluster of several types of NK cells, and a $CD127^+$ ILC cluster with cells expressing markers corresponding to ILC1, ILC2, $CD45RA^{high}$ ILC3, subsets of several types of $CD56^+$ and $CD56^-$ ILC3 [2,22] and a $CD161^-$ ILC3-like population [23]. In addition, several unrecognized cell clusters with a $Lin^-CD7^+CD127^-CD45RO^+CD56^+$ phenotype [referred to as intermediate ILC (int-ILC) hereafter] were identified which clustered between the NK cells and $CD127^+$ ILCs (**Fig. 1, C-E**). While the majority of these int-ILCs (6.6% of ILCs ± 2.3%) were $CD8a^-$, a smaller related population (3.0% ± 1.6%) was $CD8a^+$ (**Fig. 1 F**). Importantly, analysis of the composition of the cluster frequencies in the individual fetal samples demonstrated that even though quantitative differences exist, most of the identified clusters, including the int-ILCs were present in all 7 samples (**Fig. 1 F**).

Together, these data indicate that all known NK and $CD127^+$ ILC cell clusters could be identified simultaneously while evidence for the existence of previously unrecognized clusters was obtained as well.

Visualization of the t-SNE computation dynamics predicts potential differentiation trajectories in the ILC compartment

The cell surface phenotype of int-ILC (i.e. $CD127^-CD45RO^+$) places them in between the $CD127^+$ ILCs and the NK cells (**Fig. 1, C-E**), suggesting potential relationships with both. To investigate this in more detail, we sought to visualize potential relationships between cell populations without prior designation of a user-defined starting cell type in silico. To this end, we exploited the ability of Cytosplore to visualize the evolution of the t-SNE map [21]. Separating the computational modelling into 6 stages revealed how distinct cell clusters were formed, while their high-dimensional similarities were projected onto a two-dimensional map,

Fig. 2. Monitoring t-SNE computation dynamics predicts potential differentiation trajectories of ILCs (**A**) t-SNE embeddings of the collective ILC single-cell data derived from 7 fetal intestines showing density features (upper row) and single cells (bottom row) at 6 stages over the course of the t-SNE computation. Colors represent the local probability density of t-SNE-embedded cells (upper row), or cluster partitions (bottom row), as described in Fig. 1 A. (**B**) t-SNE embeddings at stage 4 of the optimization phase as described in panel A. Colors of the cells represent ArcSinh5-transformed expression values of indicated markers. (**C**) Left panel: t-SNE embedding at stage 4 as in panel A. Colors represent density features and black encirclement indicates the trajectory of cells along the CD56 expression continuum shown in panel B. Right panel: Wanderlust graph (trajectory 0-1.0) of the CD56 positive cells in the left panel showing median ArcSinh5-transformed expression of CD8a, CD45RO, CD45RA, CD7, CD3, CD56, CD117, CD127 and CRTH2 from the $CD8a^-$ int-ILCs (shaded red box) via the $CD8a^+$ int-ILC (shaded yellow box) to NK cells (shaded blue box), and from the $CD8a^-$ int-ILCs to ILC3s (shaded green box). The rainbow color bar indicates relative cell density.

and linked to each other based on marker expression profiles (**Fig. 2 A**). Since the initial positions in the t-SNE map are assigned randomly, at the first stage of the t-SNE computation all cells were unordered around a single density peak. Shortly thereafter the CD34$^+$ lymphoid precursor cells separated from the other cells (stage 2) and the first formation of the NK and CD127$^+$ ILC clusters became apparent (stage 2 and 3). These early events were based on relatively large and highly discriminatory differences in the expression profiles between cell clusters, like the unique combination of CD34 and HLA-DR expression by CD34$^+$ cells. At stage 4 of the t-SNE computation the int-ILC cluster was positioned in the center with several distinct strands of cells forming trajectories towards the NK, CD27$^+$ ILC1, KLRG-1$^+$ ILC2 and CD103$^+$ ILC3 clusters. In addition, a trajectory between the ILC2 and ILC3 clusters was visible (stage 4). Furthermore, cells from the CD8a$^-$ int-ILC population connected via the CD8a$^+$ int-ILC population with NK cells, further supporting the notion that these two CD8a$^-$ and CD8a$^+$ int-ILC populations are highly related (**Fig. 2 A and Fig. S2 B**). At the final stage of the t-SNE computation the 34 clusters were defined while the connections between the individual clusters were less clear as the t-SNE algorithm eventually assigns cells in between two clusters to either one of the two. Individual marker expression patterns at stage 4 of the t-SNE computation gave insight into the separations of and the connections between clusters (**Fig. 2 B**). Here, the NK cluster was characterized by the co-expression of CD45RA, CD56, CD122 and NKp46 while the CD127$^+$ ILC cluster expressed CD45RO, CD117, CD127, CD25 and to a lesser extent CCR6 and CD103. Similarly, connections between int-ILC to ILC1, ILC2, ILC3 and NK cells were marked by (gradients of) expression of CD27, KLRG-1, CD103 and CD56, respectively. The absence of CD45RA, CD127, and CCR6 in combination with the presence of CD45RO and CD56, and divergent expression of CD117, CD122 and CD25, positioned the int-ILC in between the NK cell and ILC clusters. Interestingly, CD56 expression linked the ILC3 to the CD8a$^-$ int-ILC, and the CD8a$^+$ int-ILC to the NK cells.

We next applied Wanderlust [24] to determine changes in marker expression along this CD56 continuum (**Fig. 2 C**), which demonstrated that the expression of CD127, CD117 and CD45RO gradually decreased while that of CD45RA and CD8a increased moving from CD8a$^-$ int-ILC to NK cells, via CD8a$^+$ int-ILC; and the expression of CD127 and CD117 gradually increased from CD8a$^-$ int-ILC to ILC3. Altogether, these results suggest that these t-SNE-based trajectories may reflect potential differentiation pathways.

Expression of cytokines, transcription factors and CD94 distinguish int-ILCs from mature CD127$^+$ ILCs and NK Cells

To further characterize the int-ILC population, we used the mass cytometry data (**Fig. S3 A**) to design a minimal antibody panel to distinguish the CD127$^-$CD45RO$^+$ int-ILCs from CD45RA$^+$ NK cells, and to identify the mature CD127$^+$ ILC types through differential expression of CD117 and CRTH2 (**Fig. 3 A**). Subsequently, we analyzed the proliferative state and examined the capacity of the subsets to

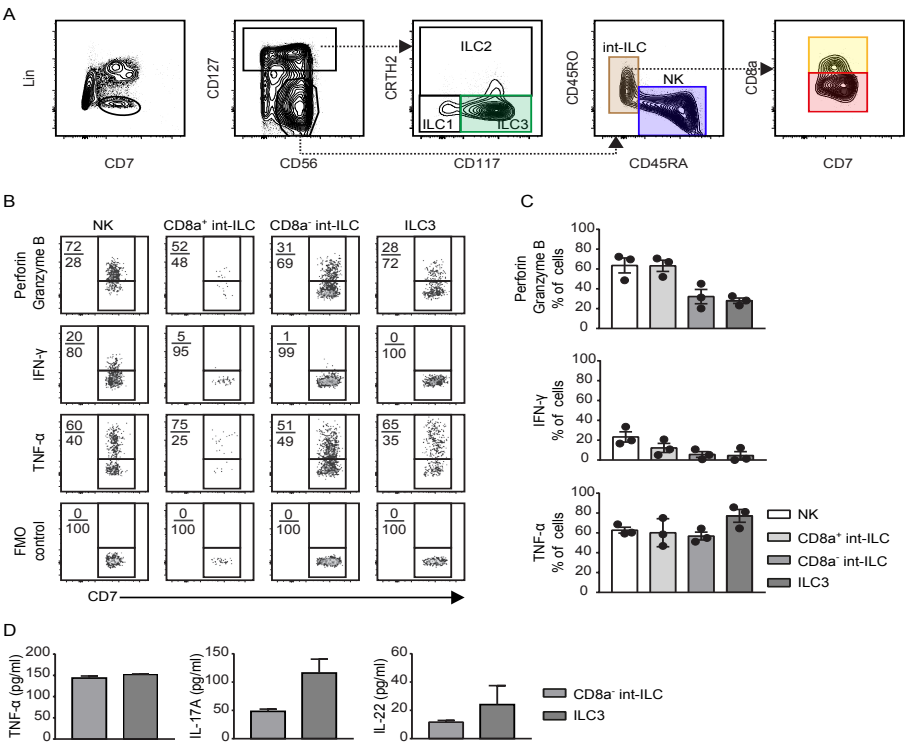

Fig. 3. Cytokine production profiles of fetal intestinal ILCs *ex vivo.* (**A**) Representative biaxial plots depicting the gating strategy for ILC1, ILC2, ILC3, NK and int-ILC subsets derived from a human fetal intestine analyzed by flow cytometry. The antibody cocktail contains lineage (Lin) markers (CD3, CD19, CD11c and CD14), and CD7, CD127, CD56, CRTH2, CD117, CD45RA, CD45RO and CD8a to allow distinction of the ILC subsets. (**B and C**) Expression of cytotoxic molecules (Perforin + Granzyme B) and cytokines (IFN-γ and TNF-α) by the indicated subsets defined in panel A after stimulation with PMA and ionomycin for 6 h. The biaxial plots (**B**) depict one representative experiment and the bar graphs (**C**) depict quantification of data obtained from 3 different human fetal intestines.Three independent experiments). FMO, fluorescence-minus-one control. Error bar shows mean ± SEM. (**D**) Bar plots depict the secretion of TNF-α, IL-17A and IL-22 by CD8a$^-$ int-ILC and ILC3, after stimulation with IL-2, IL-1β and IL-23 for 4 days, using Luminex bead-based assay of an experiment with 3 intestines and duplicate wells. (Two independent experiments). Error bar shows mean ± SD.

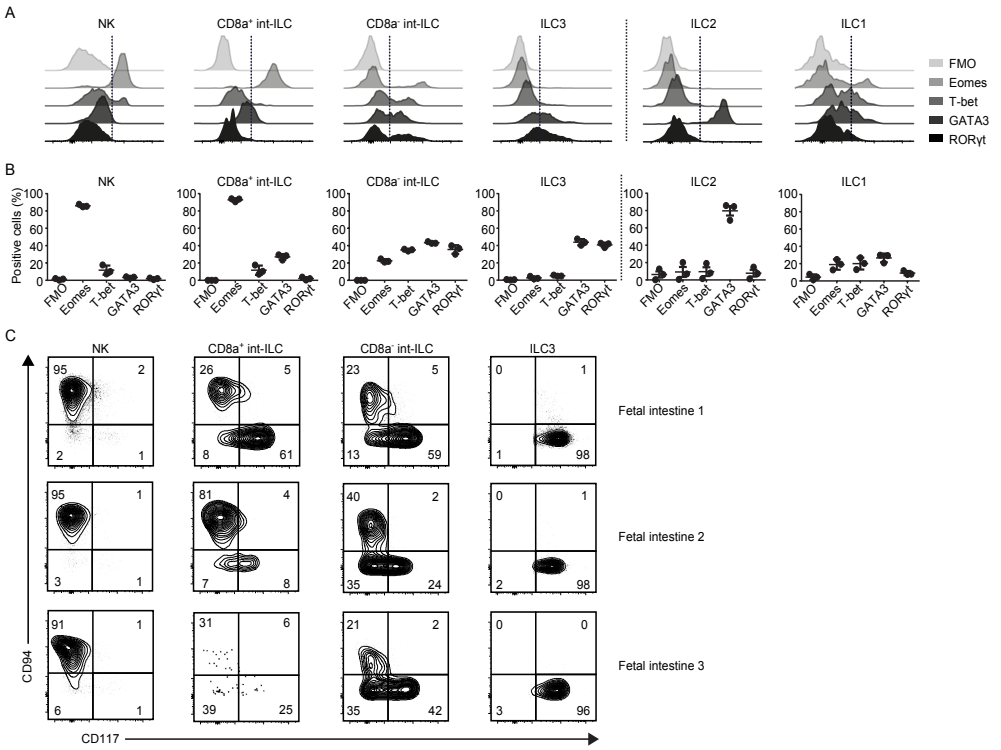

Fig. 4. Transcription factors and CD94 expression profiles of fetal intestinal ILCs *ex vivo*. (**A and B**) Flow cytometric determination of the expression of the transcription factors Eomes, T-bet, GATA3 and RORγt by the indicated ILC subsets as defined in Fig. 3 A. Histograms (**A**) depict the results with one representative human fetal intestine and the graphs (**B**) depict quantification of data obtained from 3 different human fetal intestines. (Three independent experiments). FMO, fluorescence-minus-one control. Error bar shows mean ± SD. (**C**) Biaxial plots showing the expression of CD94 and CD117 by the indicated subsets. Results on 3 human fetal intestines are shown. (Three independent experiments).

produce cytokines and express markers linked to cytolytic potential by flow cytometry. For the former we stained the cells with the proliferation marker Ki-67 ex vivo. The highest percentage of Ki-67 positive cells was present in the CD8a$^+$ int-ILC population (43.9%) while on average 20% of cells in the other subsets were Ki-67 positive (**Fig. S3 B**). Upon stimulation with PMA and ionomycin Perforin/Granzyme B was detectable in all subsets, but more profoundly in the NK cells and CD8a$^+$ int-ILCs compared with the CD8a$^-$ int-ILCs and ILC3s (**Fig. 3, B and C**). Moreover, all subsets expressed high levels of TNF-α, while IFN-γ was detected mainly in the NK cells and CD8a$^+$ int-ILCs but hardly in the CD8a$^-$ int-ILCs and ILC3s (**Fig. 3, B and C**). ILC2s expressed IL-4, IL-5 and IL-13, but ILC1s very little IFN-γ (not shown). In contrast, IL-4, IL-5 and IL-13 was undetectable in any of the other subsets (not shown) while IL-17A and IL-22 expression was higher by

ILC3s than CD8a$^-$ int-ILCs (**Fig. 3 D**).

Next we determined the expression of key transcription factors associated with ILC development and phenotype. The expression of ID2, TCF7, AHR, NFIL3, ZBTB16 and TOX did not discriminate between the subsets (**Fig. S3 C**). In line with previous work [25], the ILC2 subset was strongly GATA3 positive and RORγt negative, while ILC3s were GATA3 and RORγt positive (**Fig. 4, A and B and Fig. S3 D**). However, we found only low levels of T-bet expression by ILC1 (**Fig. 4, A and B**). Notably, both mature NK cells and CD8a$^+$ int-ILCs expressed high levels of Eomes (**Fig. 4, A and B and Fig. S3, E and F**). In contrast, the CD8a$^-$ int-ILCs were heterogeneous with respect to the expression of the 4 transcription factors which were all expressed by a proportion of the cells (**Fig. 4, A and B**), an expression profile that does not correspond to those found in mature CD127$^+$ ILCs. Furthermore, multiple lineage transcription factors could be simultaneously expressed by CD8a$^-$ int-ILCs, such as T-bet and GATA3 (26.1% of CD8a$^-$ int-ILCs) (**Fig. S3, G-I**). Finally, the frequency of cells expressing Eomes decreased along the potential differentiation trajectory linking the NK cells to CD8a$^+$ int-ILCs, CD8a$^-$ int-ILCs and ILC3s, while that of RORγt increased (**Fig. 4, A and B**).

To investigate the relationship between the int-ILCs, NK cells and ILC3s further, we evaluated the expression of CD62L, CD57, CD5 and the NK cell-associated C-type lectin receptor CD94. Here, expression of CD62L, CD57 and CD5 was almost lacking and did not discriminate between the subsets (not shown) while CD94 expression was high on NK cells but virtually absent from ILC3s (**Fig. 4 C**), in agreement with previous studies [2,10]. In contrast, only part of the int-ILCs were CD94 positive with a higher expression level of CD94 on CD8a$^+$ int-ILCs compared to CD8a$^-$ int-ILCs (**Fig. 4 C**), a result in line with the lower expression of Eomes in the latter. Furthermore, in contrast with CD94$^-$ cells, CD94$^+$ cells lacked the expression of CD117, similar to mature NK cells (**Fig. 4 C**).

Together, these data indicate that the int-ILC subset is distinct from mature ILCs, where the expression pattern of the cytokines, CD94 and transcription factors link the CD8a$^+$ int-ILCs to NK cells and the CD8a$^-$ int-ILCs to ILC3s.

int-ILC can differentiate into CD45RA$^+$ NK cells

To test the hypothesis that the int-ILC subset may differentiate into CD127$^+$ ILCs and/or NK cells, we first purified the CD8a$^-$ int-ILCs by flow cytometry (**Fig. 5 A**) and performed functional differentiation assays by co-culturing these with OP9 stromal cells expressing the Notch ligand Delta-like 1 (OP9-DL1). After 7 days of culture in medium containing stem cell factor (SCF), IL-7, IL-2 and IL-15

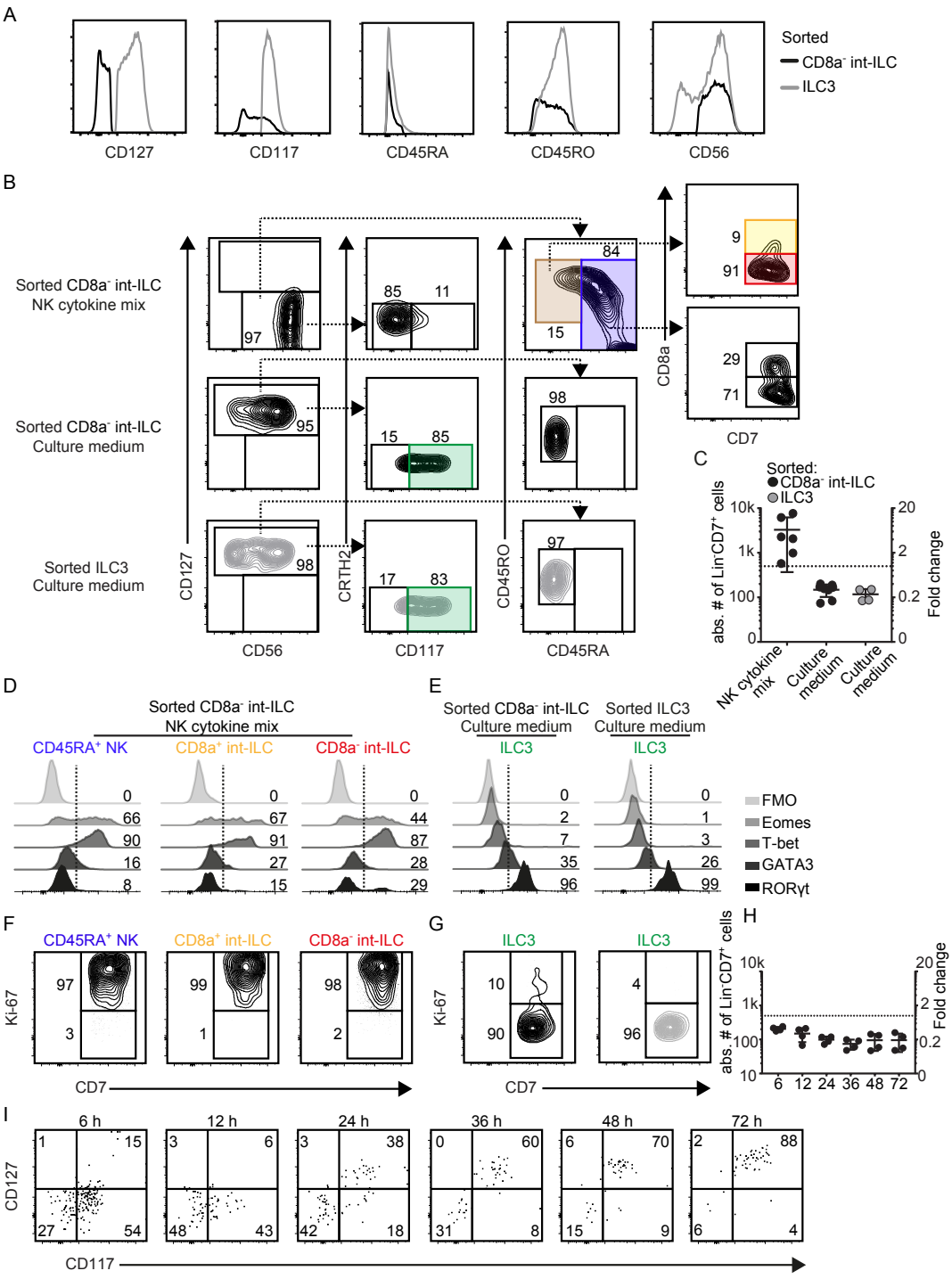
A
CD127
CD117
CD45RA
CD45RO
CD56
Sorted
CD8a- int-ILC
ILC3
B
Sorted CD8a- int-ILC
NK cytokine mix
Sorted CD8a- int-ILC
Culture medium
Sorted ILC3
Culture medium
CD127
CD56
CRTH2
CD117
CD45RO
CD45RA
CD8a
CD7
C
Sorted:
CD8a- int-ILC
ILC3
abs. # of Lin-CD7+ cells
Fold change
NK cytokine mix
Culture medium
Culture medium
D
Sorted CD8a- int-ILC
NK cytokine mix
CD45RA+ NK
CD8a+ int-ILC
CD8a- int-ILC
E
Sorted CD8a- int-ILC
Culture medium
Sorted ILC3
Culture medium
ILC3
FMO
Eomes
T-bet
GATA3
RORγt
F
CD45RA+ NK
CD8a+ int-ILC
CD8a- int-ILC
Ki-67
CD7
G
ILC3
ILC3
Ki-67
CD7
H
abs. # of Lin-CD7+ cells
Fold change
6 12 24 36 48 72
I
6 h
12 h
24 h
36 h
48 h
72 h
CD127
CD117

(hereafter referred to as NK cytokine mix), the majority of the int-ILCs acquired a CD45RA$^+$ phenotype (**Fig. 5 B**) and expanded substantially (**Fig. 5 C**). Also, these cells upregulated CD94 (42% positive) (**Fig. S4 A**) and displayed expression of Eomes and/or T-bet, but no RORγt or GATA3 (**Fig. 5 D**), all similar to mature NK cells. Furthermore, part of these cells expressed CD8a (**Fig. 5 B**), a marker expressed by most fetal NK cells ex vivo (**Fig. 2 B**), where most of the CD8a$^+$ cells displayed the highest expression of Eomes (**Fig. S4 B**). Moreover, a small fraction of generated cells maintained the CD45RA$^-$CD45RO$^+$ int-ILC phenotype and a fraction of them also acquired CD8a (**Fig. 5 B**). In line with the suggested differentiation trajectory (**Fig. 2 C**), the expression of ILC3-associated RORγt decreased from the CD8a$^-$ int-ILCs to CD8a$^+$ int-ILCs to CD45RA$^+$ NK cells while all populations expressed high levels of NK cell-associated Eomes and/or T-bet (**Fig. 5 D**). Also, the cells became uniformly Ki-67 positive (**Fig. 5 F**), consistent with the observed increase in cell numbers (**Fig. 5 C**). As similar results were obtained when purified CD8a$^-$ int-ILCs were co-cultured with OP9 stromal cells without Delta-like 1, Notch signalling appears not to be involved (**Fig. S4 C**). In addition, upon culture on OP9-DL1 purified CD8a$^+$ int-ILCs also acquired the CD45RA$^+$ NK cell phenotype, maintained CD8a expression and expressed high levels of CD94 (84% positive) (**Fig. S4 D**). Finally, purified CD8a$^-$ int-ILCs co-cultured with OP9-DL1

Fig. 5. int-ILC can differentiate into CD45RA$^+$ NK cells and ILC3. (**A**) Representative histograms depicting the expression of CD127, CD117, CD45RA, CD45RO, CD56 by flow cytometry-purified CD8a$^-$ int-ILCs (black line) and ILC3s (grey line) from human fetal intestines. Data are representative of six independent experiments. (**B-G**) Purified CD8a$^-$ int-ILCs and ILC3s were co-cultured in 96 well plates at 500 cells/well with irradiated OP9-DL1 stromal cells for 7 days with culture medium alone or supplemented with SCF, IL-7, IL-2, IL-15 (referred to as NK cytokine mix). Generated cells were analyzed by flow cytometry. Duplicated wells were included for each condition. Representative plots show a single duplicate. (**B**) Representative biaxial plots depict the phenotypes of generated Lin$^-$CD7$^+$ cells based on the gating strategy for ILC1, ILC2, ILC3, NK and int-ILC subsets as shown in Fig. 3 A, for three different combinations of sorted cell populations (int-ILC in black contours, ILC3 in grey contours) and culture conditions as indicated. (Three to five independent experiments). (**C**) Quantification of the generated Lin$^-$CD7$^+$ cells in panel B in absolute cell number (left axis) and fold change (right axis) compared to the number of initially sorted cells (dashed line). (Two to four independent experiments). Error bar shows mean ± SD. (**D and E**) Histograms depict the expression of transcription factors Eomes, T-bet, GATA3 and RORγt by the indicated subsets generated from (**D**) sorted CD8a$^-$ int-ILCs with NK cytokine mix and (E) sorted CD8a$^-$ int-ILCs or ILC3s with culture medium. Numbers indicate the percentage of positive cells. FMO, fluorescence-minus-one control. Combined data on 5 human fetal intestines. (**F and G**) Biaxial plots depict the expression of Ki-67 by indicated subsets generated from the combinations of sorted cell populations (int-ILC in black contours, ILC3 in grey contours) and culture conditions as in panel D and E. Combined data on 5 human fetal intestines. (**H-I**) Purified CD8a$^-$ int-ILCs were co-cultured at 500 cells/well with irradiated OP9-DL1 stromal cells in culture medium and harvested at the time points indicated in hours. Duplicated wells were included in each experiment. (Two independent experiments). (**H**) Quantification of the generated Lin$^-$CD7$^+$ cells in absolute cell number (left axis) and fold change (right axis) compared to the number of initially sorted cells (dashed line). (**I**) Representative biaxial plots show the expression of CD127 and CD117 by the generated Lin$^-$CD7$^+$ cells.

and IL-15 cytokine only similarly expanded (not shown), acquired CD45RA, upregulated CD94 (41% positive), and became in part CD8a positive (**Fig. S4 E**). However, under these conditions approximately 60% of these generated cells remained CD117$^+$ (**Fig. S4 E**), suggesting an incomplete conversion to the mature NK cell phenotype [26]. Together these data indicate that in the presence of NK cytokines, proliferative CD45RA$^+$ NK cells are generated from int-ILC.

CD8a$^-$ int-ILC can differentiate into ILC3

In marked contrast, when purified CD8a$^-$ int-ILCs and ILC3s (**Fig. 5 A**) were individually co-cultured with OP9-DL1 in cytokine-free culture medium, the ILC3s retained their phenotype while the CD8a$^-$ int-ILCs acquired an ILC3 phenotype as they became CD127$^+$CD117$^+$ (**Fig. 5 B**), remained CD45RA$^-$CD45RO$^+$ (**Fig. 5 B**) and CD8a$^-$ (not shown), in the absence of cell expansion and proliferation (**Fig. 5, C and G**). This phenotype was also stable during prolonged culture (**Fig. S4 F**). In addition, these cells homogeneously expressed RORγt, but no Eomes or T-bet (**Fig. 5 E**), suggesting an established ILC3 population [2]. As similar results were observed when we co-cultured the CD8a$^-$ int-ILCs with OP9 stromal cells that lacked Notch ligand Delta-like 1, Notch signalling appears not to be involved (**Fig. S4, G and H**). Unlike CD8a$^-$ int-ILCs and ILC3s, both purified CD45RA$^+$ NK cells and CD8a$^+$ int-ILCs did not survive under these conditions. To exclude that the generation of ILC3 by int-ILCs was due to outgrowth of contaminating ILC3s, we determined cell numbers and the acquisition of CD127 and CD117 at various time points during culture. After 24 and 72 h of culture, 38% and 88% of purified CD8a$^-$ int-ILCs had acquired both CD127 and CD117, respectively, while no increase in cell numbers was observed (**Fig. 5, H and I**). Together with the observation that only a very small proportion of both the purified mature ILC3s and differentiated ILC3s from int-ILCs were Ki-67$^+$ (**Fig. 5 G**), this indicates that it is highly unlikely that selective outgrowth of contaminating ILC3s could explain the appearance of cells with an ILC3 phenotype in the CD8a$^-$ int-ILC/OP9 co-cultures. Thus, these results indicate that the CD8a$^-$ int-ILC population can differentiate into ILC3 in vitro.

Differentiation properties of CD8a$^-$ int-ILC subpopulations

By the differential expression of CD94 and CD117 three distinct CD8a$^-$ int-ILC subpopulations could be distinguished: CD94$^+$CD117$^-$, CD94$^-$CD117$^-$ and CD94$^-$CD117$^+$ (**Fig. 4 C**). We therefore investigated whether these subsets could differentiate into either NK cells or ILC3s in vitro. For this purpose, we first examined the expression of transcription factors (**Fig. 6, A and B**). This revealed that Eomes was primarily present in the CD94$^+$CD117$^-$ subset while RORγt

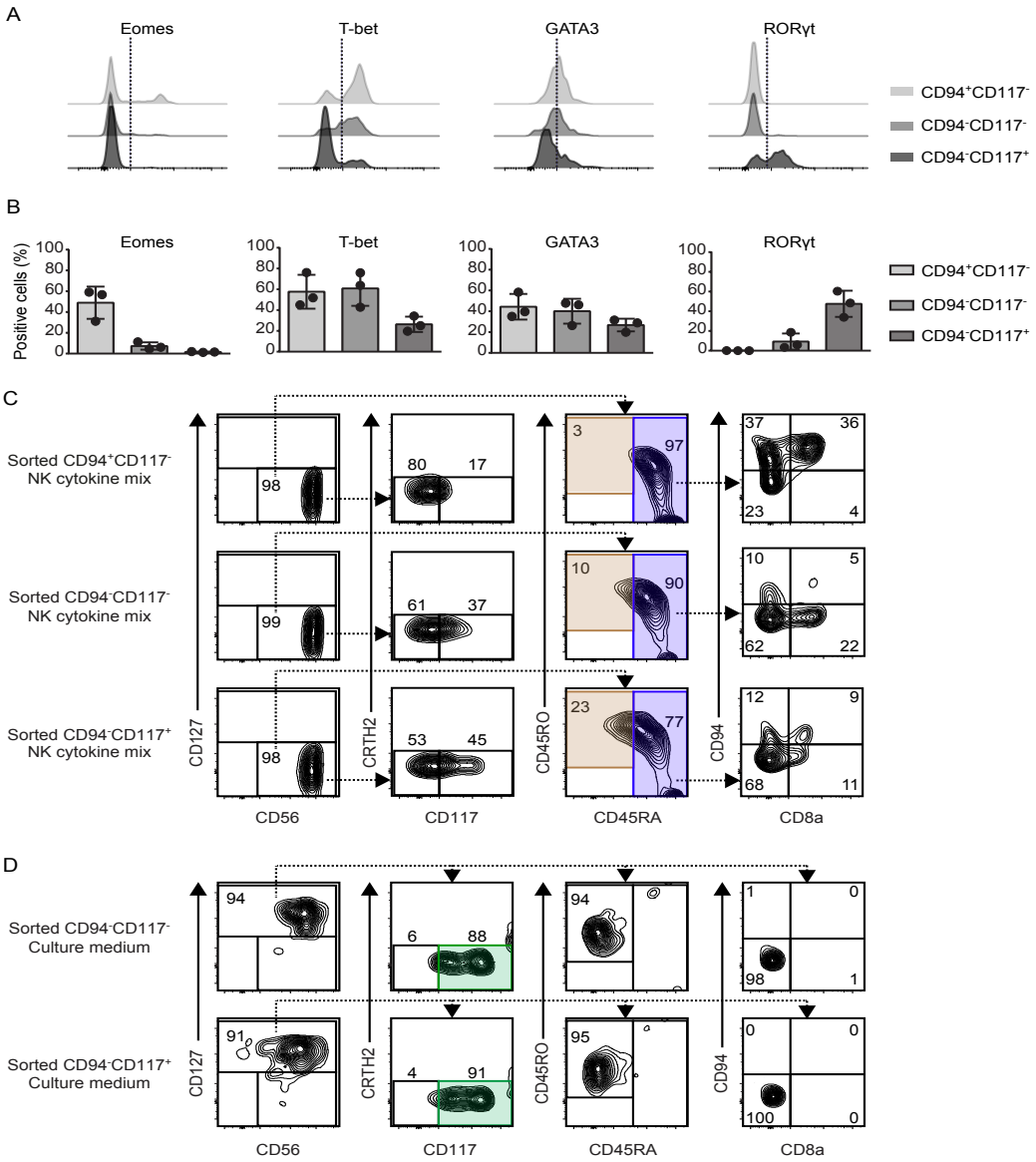

Fig. 6. Distinct differentiation properties of CD8a$^-$ int-ILC subpopulations. (**A and B**) Expression of the transcription factors Eomes, T-bet, GATA3 and RORγt by the indicated subpopulations of CD8a$^-$ int-ILC *ex vivo*. Histograms (**A**) depict the results with one fetal intestine and the graphs (**B**) depict quantification of data obtained from 3 intestines. (Two independent experiments). Error bar shows mean ± SD. (C and D) Purified CD94$^+$CD117$^-$CD8a$^-$ int-ILC, CD94$^-$CD117$^-$CD8a$^-$ int-ILC and CD94$^-$CD117$^+$CD8a$^-$ int-ILC populations were co-cultured in 96 well plates at 500 cells/well with irradiated OP9-DL1 stromal cells for 7 days with (**C**) culture medium supplemented with NK cytokine mix or (**D**) culture medium alone. Generated cells were analyzed by flow cytometry. Representative biaxial plots depict the phenotypes of the generated Lin$^-$CD7$^+$ cells based on the gating strategy for ILC1, ILC2, ILC3, NK and int-ILC subsets as shown in Fig. 3 A, for the five combinations of cell populations and culture conditions indicated. Duplicated wells were included in each condition. Representative plots show a single duplicate. (Three to four independent experiments).

expression was most pronounced in the CD94$^-$CD117$^+$ subset. In addition, all subsets expressed GATA3 and T-bet, where T-bet expression was most pronounced by the CD117$^-$ subsets. Together, these results explain the heterogeneity in the expression of transcription factors by CD8a$^-$ int-ILCs and position the CD94$^-$CD117$^-$ subset in between the CD94$^+$CD117$^-$ and CD94$^-$CD117$^+$ subsets.

Next, we purified CD94$^+$CD117$^-$, CD94$^-$CD117$^-$, and CD94$^-$CD117$^+$ subsets individually and co-cultured them with OP9-DL1 stromal cells with either NK cytokine mix or cytokine-free medium. In the presence of NK cytokine mix (**Fig. 6 C**), virtually all of the CD94$^+$CD117$^-$ cells acquired the CD45RA$^+$ NK cell phenotype, maintained expression of high levels of CD94 (76%), acquired CD8a expression (43%) and expanded substantially (12-fold; not shown). Similarly, most of the CD94$^-$CD117$^-$ cells and the majority of the CD94$^-$CD117$^+$ cells also acquired the CD45RA$^+$ NK cell phenotype, acquired expression of CD94 (17% and 25%, respectively) and CD8a (24% and 16%, respectively), and expanded (9-fold and 7-fold, respectively; not shown). In contrast, in cytokine-free medium (**Fig. 6 D**) both the CD94$^-$CD117$^-$ and CD94$^-$CD117$^+$ int-ILCs acquired an ILC3 phenotype as they became CD127$^+$, remained CD45RO$^+$CD45RA$^-$CD94$^-$CD8a$^-$ and acquired or increased the levels of CD117 expression, respectively (**Fig. 6 D**). Similar to CD8a$^+$ int-ILCs and CD45RA$^+$ NK cells the CD94$^+$CD117$^-$ int-ILCs did not survive under these conditions.

Taken together, in these in vitro experiments all three subpopulations of the CD8a$^-$ int-ILCs can differentiate into NK cells, whereas the CD94$^-$CD117$^-$ and CD94$^-$CD117$^+$ cells, but not the CD94$^+$CD117$^-$ cells can differentiate into ILC3s.

Discussion

Numerous studies have reported substantial heterogeneity in the ILC compartment [2,22]. In our mass cytometry-based approach the NK, ILC1, ILC2 and ILC3 subsets could be readily identified in the human fetal intestine as well as substantial variability within those subsets, results that were highly consistent in several samples analyzed. Based on the marker expression profiles, we identified a large number of distinct NK cell clusters, whose biological significance needs to be investigated in the future studies. In addition, we found a small CD27$^+$ ILC cluster that matches ILC1 criteria [1,27]. However, in contrast to findings from Bernink et al. (2013), but in line with other studies [22,23], only few of these ILC1s expressed T-bet. Furthermore, two additional CD127$^+$ ILC1-like clusters were identified which clustered with the NK cells due to the expression of several NK cell-associated markers, including

CD45RA, CD56, CD8a and NKp46. Consistent with previous reports [2,13,22] the ILC3 compartment was most frequent and heterogeneous, including CD45RO$^+$ ILC3, CD45RA$^+$ ILC3, HLA-DR$^+$ ILC3 and CD56$^{+/-}$ ILC3 clusters. Further studies will be required to clarify the potential functional significance of observed heterogeneity in the ILC3 lineage. We could not distinguish LTi cells from ILC3s as no specific cell surface marker for human LTi cells was available at the time we performed our analysis. Moreover, while most of the human ILCs described express CD161 [1,2], we also detected a recently described CD161$^-$CD117$^+$ ILC3-like cluster that clustered with the CD127$^+$ ILCs [23]. In addition, we identified two previously unknown CD8a$^+$ counterparts of ILC3s that warrants further investigation. We also observed a rare CD34$^+$CD45RA$^+$CD117$^+$ population that resembles the CD34$^+$ precursors recently described in human tonsils and intestines after birth [9,10].

Finally, we identified a Lin$^-$CD7$^+$CD127$^-$CD45RO$^+$CD56$^+$ group of cells which by unbiased clustering were positioned between the CD45RA$^+$ NK cells and CD127$^+$ ILCs, and were termed int-ILC. While in previous studies [1,2] such CD56$^+$CD127$^-$ cells were classified as NK cells, the simultaneous use of CD45RA and CD45RO allowed us to distinguish these CD45RO$^+$ cells from the CD45RA$^+$ NK cells. It is important to note that these int-ILCs display variable expression of several surface markers, including CD8a, CD94, CD117, CD122, CD25, CD27, KLRG-1 and CD103, indicating that they are not a homogenous group of cells. Their unique position in between the NK cells and CD127$^+$ ILCs, however, prompted us to investigate potential relationships between these cell clusters.

In recent years, several studies have explored developmental pathways by applying computational approaches on mass cytometry datasets. Wanderlust, accurately predicted B cell lymphopoiesis [24] and Wishbone was found to recover the T cell developmental pathway [28] at single-cell resolution. However, Wanderlust is not suitable to predict multi-lineage differentiation trajectories. While Wishbone can be used to identify bifurcating developmental trajectories, it needs the designation of a user-defined precursor cell type. As we wished to investigate potential developmental relationships without pre-assumptions we developed a novel computational approach to visualize the evolution of the t-SNE map over the course of the optimization. t-SNE is a non-linear dimensionality reduction algorithm which projects the high-dimensional similarities onto a two-dimensional map based on the concurrent marker expression profiles [19]. Here t-SNE not only employs bimodal distribution patterns but also incorporates gradients of the expression of cellular markers and therefore offers superior resolution. Importantly, the Cytosplore framework [21] can visualize every iteration by making use of the A-tSNE [29]. This allowed us to analyze potential relationships between

the int-ILC, ILC1, ILC2, ILC3 and NK clusters through visualization of gradients along putative differentiation trajectories. Such gradients are clearly visible in our Cytosplore analysis (**Fig. 2**) and contribute to the generation of cell clusters. Our current results indicate that at least some of those gradual changes in marker expression profiles correlate with differentiation pathways of immune subsets. Consistent with the observed plasticity among ILCs [13,15], the analysis revealed a clear trajectory between the ILC2 and ILC3 clusters. This may imply that the CD103$^-$ ILC2 can differentiate into CD103$^+$ ILC3 locally depending on physiological or pathological conditions. Alternatively, the fetal ILC2s may leave the intestine, in line with previous reports that ILC2s can be found in the peripheral blood [30] but are virtually absent in the human intestine after birth [13]. In addition, a trajectory within the CD56$^+$ cell compartment was revealed, where the CD8a$^-$ int-ILC was connected with the CD56$^+$ ILC3 on one side and with the CD8a$^+$ int-ILC and the NK cells on the other. Importantly, while the above analysis was performed on the innate cell population present in the 7 fetal intestines collectively, similar relationships between cell populations were revealed when the innate cell compartment of each fetal sample was analyzed individually, attesting to the robustness of the approach (**Fig. S2 B**).

The putative link between the int-ILC and the mature ILC and NK cells is further strengthened by several other observations. First, both the cytokine production profiles and CD94 expression profile ex vivo link the CD8a$^+$ int-ILCs to NK cells and the CD8a$^-$ int-ILCs to the ILC3s. Second, the expression pattern of the transcription factors by int-ILCs is heterogeneous with features of both NK cells (Eomes and T-bet) and ILC3s (GATA3 and RORγt) where the CD8a$^+$ int-ILCs resemble the NK cells while the CD8a$^-$ int-ILCs are closer to CD127$^+$ ILCs. Finally, in the OP9-based co-culture system, in the presence of NK cytokines purified int-ILC expanded and displayed a CD45RA$^+$Eomes$^+$/T-bet$^+$ NK cell phenotype while in the absence of cytokines the cells did not expand but acquired a stable CD127$^+$CD117$^+$RORγt$^+$ ILC3 phenotype.

Further dissection of the CD8a$^-$ int-ILC compartment demonstrated the existence of three distinct subpopulations based on differential expression of CD94 and CD117: CD94$^+$CD117$^-$, CD94$^-$CD117$^-$ and CD94$^-$CD117$^+$. In our in vitro experiments both the Eomes-expressing CD94$^+$CD117$^-$ and non-Eomes-expressing CD94$^-$CD117$^-$ and CD94$^-$CD117$^+$ subpopulations could differentiate into CD45RA$^+$ NK cells when cultured with NK cytokine mix. Furthermore, the differentiation into CD45RA$^+$ NK cells was most efficient in the case of the CD94$^+$CD117$^-$ cells and least for the CD94$^-$CD117$^+$ cells, compatible with a model where the CD94$^+$CD117$^-$ cells are positioned close to NK cells, the CD94$^-$CD117$^+$ cells most distant and the CD94$^-$

CD117$^-$ cells in between. The acquisition of CD8a by the CD94$^-$CD8a$^-$ int-ILCs in these cultures indicates that the CD8a$^+$ int-ILC may also be an intermediate stage towards NK cell differentiation. In the absence of cytokines CD117$^+$CD127$^+$ ILC3-like cells could be generated from both CD94$^-$CD117$^+$ and CD94$^-$CD117$^-$ cells but not from CD94$^+$CD117$^-$ cells. Together this indicates that CD94$^+$CD117$^-$ cells can exclusively differentiate into NK cells while the other two populations can differentiate into both NK cells and ILC3s, at least under the in vitro conditions employed.

In the absence of cytokines the int-ILC changed into ILC3-like cells without signs of cell expansion, cell division or cell death, arguing that the generation of ILC3 from the int-ILC is not due to selective outgrowth of contaminating ILC3s. In agreement, we did not observe any proliferative response of flow cytometry-purified ILC3 under the same experimental conditions.

In mice, it has been shown that developmental hierarchy of ILCs goes from the common lymphoid progenitor (CLP) to mature ILCs via α4β7-expressing lymphoid progenitor (αLP), early innate lymphoid progenitor (EILP), common helper ILC progenitor (CHILP), and the ILC precursor (ILCP) [7]. Here EILP has been distinguished from other progenitors by the lack of CD127 and ILC lineage-specific transcription factors [31], while the ILCP exhibits co-expression of transcription factors associated with ILC1, ILC2 and ILC3 subsets [32]. Finally, a murine fetal transitional CD127$^+$ ILCP (ftILCP) has been identified in the intestine which expresses varying amount of T-bet, GATA3 and RORγt [33]. In humans, two studies have shown that ILC3s can be generated from RORγt$^+$CD34$^+$ progenitors from tonsils and intestines [9,10] but little is known about the intermediate stages. Interestingly, Scoville et al. (2016) generated both NK cells and the three types of helper ILCs from these CD34$^+$ progenitors in vitro, however, the generated cells did not express CD127 but rather CD161 and intracellular ILC-related cytokine profiles. Also, a NK cell lineage-restricted CD34$^+$ progenitor was identified in the human fetal liver and bone marrow [34]. In contrast, CD127$^-$ int-ILC in our study express CD45RO and variable levels of Eomes, T-bet, GATA3 and RORγt, but no CD34 and CD45RA, markers expressed by most human progenitors. Also, with our mass cytometry approach we have been unable to identify cells with an int-ILC phenotype in the human fetal liver and fetal spleen (not shown), indicating that the int-ILC may specifically reside in mucosal tissues. Together, the cell surface phenotype, tissue distribution and transcription factor profiles of CD127$^-$ int-ILC suggests that these cells are distinct from previously identified ILC progenitors and may be in an intermediate differentiation stage among ILC lineages. Finally, we observed that the ILC3s and NK cells derived from the CD8a$^-$ int-ILC could partly revert their

phenotype upon prolonged culture indicating that the int-ILC may represent an intermediate between two plastic lineages (not shown).

It has been shown that environmental cues including OP9/OP9-DL1 stromal cells and cytokines such as IL-7 and SCF play an important role in driving ILC3 differentiation [9,10,35]. While the addition of SCF and IL-7 did promote significant expansion of the CD8a$^-$ int-ILCs, they did not differentiate into other types of cells (not shown). Instead, the differentiation of CD8a$^-$ int-ILCs toward ILC3s occurred in cytokine-free medium. In mice, Notch signalling for ILC3 development is necessary in adults but not in fetuses [8], while in humans, the differentiation of CD34$^+$ progenitors to ILC3s can occur without Notch signalling [9,10]. Consistent with these observations the generation of ILC3s from the CD8a$^-$ int-ILCs was Notch independent.

In conclusion, we delineated the heterogeneity of ILCs in the human fetal intestine and developed a computational model to predict potential differentiation trajectories based on mass cytometry data. This allowed the identification of a previously unidentified innate cell cluster that harbors cells that can differentiate into NK cells and ILC3-like cells in vitro. This may provide plasticity in the human fetal intestine in response to (external) stimuli.

Material and methods

Human fetal intestine and cell isolation

Human fetal intestines from elective abortions were collected after informed consent. Approval by the medical ethical commission of the LUMC (protocol P08.087) was obtained in accordance with the local ethical guidelines and the declaration of Helsinki. The gestational age ranged from 16 to 22 weeks. Single cell suspensions from fetal intestines were prepared as previously described. Briefly, the mesentery, colon part and meconium were removed from the fetal intestine. The intestines were then cut into small fragments and treated with 1 mM 1,4-Dithiothreitol (Fluka) in 15 mL of HBSS (Sigma-Aldrich) for 2 x 10 min (replacing buffer) at room temperature (rT) to dissolve the mucus and subsequently with 1 mM EDTA (Merck) in 15 mL of HBSS under rotation for 2 x 1 h (replacing buffer) at 37 °C to separate the epithelium from the lamina propria fraction. To obtain single-cell suspensions from the lamina propria, the intestines were rinsed with HBSS and incubated with 15 mL Iscove's Modified Dulbecco's Medium (IMDM; Lonza) supplemented with 10% FCS, 10 U/mL collagenase IV (Worthington), 200

µg/mL DNAse I grade II (Roche Diagnostics), at 37 °C overnight, after which cell suspensions were filtered through a 70 µm nylon cell strainer. Finally, the immune cells were isolated with a Percoll (GE Healthcare) gradient and stored in liquid nitrogen.

Mass cytometry antibody staining and data acquisition

Details on antibodies used are listed in **Table S1**. Conjugation of the purified antibodies with metal reporters was performed with the MaxPar X8 antibody labeling kit (Fluidigm Sciences) according to the manufacturer's instruction. Procedures for mass cytometry antibody staining and data acquisition were carried out as previously described [18]. Briefly, cells from fetal intestinal lamina propria were thawed and incubated with 1 mL 500x diluted 500 µM Cell-ID intercalator-103Rh (Fluidigm Sciences) for 15 min at rT to identify dead cells. Cells were then stained with metal-conjugated antibodies for 45 min at rT. After staining, cells were labeled with 1 mL 1,000x diluted 125 µM Cell-ID intercalator-Ir (Fluidigm Sciences) to stain all cells in MaxPar Fix and Perm Buffer (Fluidigm Sciences) overnight at 4 °C. Finally, cells were acquired by CyTOF 2™ mass cytometer (Fluidigm Sciences). Data were normalized by using EQ Four Element Calibration Beads (Fluidigm Sciences) with the reference EQ passport P13H2302 during the course of each experiment.

Mass cytometry data analysis

The biaxial plots showing antibody staining patterns in **Fig. S1** were generated in Cytobank [36]. Data for single, live $CD45^+$ cells gated from each fetal intestine individually using Cytobank [36] as shown in **Fig. S1 A**, were sample tagged and hyperbolic arcsinh transformed with a cofactor of 5 prior to t-SNE analysis. The 907 clusters shown in **Fig. S1 C** were identified by analyzing the entire immune system ($CD45^+$ cells) using the t-SNE-ACCENSE analysis pipeline as described before [18]. Next, t-SNE was performed for the ILC dataset using A-tSNE [29] in Cytosplore [21]. t-SNE was carried out with default parameters (perplexity: 30; iterations: 1000). All t-SNE plots were generated in Cytosplore. Hierarchical clustering of the heatmap was created with Pearson Correlation and average linkage clustering in MultiExperiment Viewer (http://www.tm4.org). Wanderlust analysis was performed on cells that were selected along the linear CD56 expression continuum at stage 4 of the t-SNE computation with the $CD56^+CD8a^+$ ILC3 cluster as starting point (as this cluster is located at the outer end of the CD56 trajectory), using Cyt in Matlab [24].

Antibodies and flow cytometry

FITC-conjugated anti-CD11c (3.9), PerCP-Cy5.5-conjugated anti-CD45RO (UCHL1), PE/Dazzle 594-conjugated anti-CD45RA (HI100), PE-Cy7-conjugated anti-CD127 (A019D5), Brilliant Violet 605-conjugated anti-CRTH2 (BM16), anti-T-bet (4B10), PE-conjugated anti-T-bet (4B10), anti-IFN-γ (4S.B3), anti-IL-5 (TRFK5), anti-IL-13 (JES10-5A2), anti-IL-17A (BL168) and anti-TNF-α (Mab11) were purchased from Biolegend. The following monoclonal antibodies were purchased from BD: FITC-conjugated anti-CD3 (SK7), anti-CD19 (4G7) and anti-CD14 (MφP9), APC-conjugated anti-CD117 (YB5.B8), APC-R700-conjugated anti-CD56 (NCAM16.2), V450-conjugated anti-CD7 (M-T701), Brilliant Violet 605-conjugated anti-CD94 (HP-3D9), PE-conjugated anti-CD94 (HP-3D9), anti-RORγt (Q21-559), anti-Ki-67 (B56), anti-Perforin (δG9), anti-IL-4 (3010.211). PE-conjugated anti-Eomes (WD1928), anti-GATA3 (TWAJ), anti-Granzyme B (GB11), and eFluor 660-conjugated anti-GATA3 (TWAJ) were purchased from eBioscience. PE-conjugated anti-IL-22 (IC7821P) was purchased from R&D systems. Pacific Orange-conjugated anti-CD8a (3B5) was purchased from Life technologies.

For the cell surface staining, cells were incubated with fluorochrome-conjugated antibodies and human FC block (Biolegend) for 30-45 min at 4 °C. The transcription factor staining was performed by using Foxp3 Staining Buffer Set (eBioscience) according to the manufacturer's instruction. For the intracellular cytokine staining/ cytotoxic molecule, cells were stimulated with 0.1 mg/mL PMA (Sigma-Aldrich) and 1 μg/mL Ionomycin (Sigma-Aldrich) for 6 h at 37 °C and GolgiPlug (BD Biosciences) was added for the final 4 h after which cells were stained by using Fixation Buffer and Intracellular Staining Perm Wash Buffer (Biolegend). Cells were acquired on an LSR II cytometer (BD Biosciences) or sorted on a FACSAria™ III sorter (BD Biosciences) based on the gating strategy as shown in **Fig. 3 A.** Data were analyzed with FlowJo V10 software.

Quantitative Real-Time PCR (RT-PCR)

RNA extraction was performed with the NucleoSpin® RNA XS kit (Macherey-Nagel). cDNA was synthesized with the High Capacity cDNA Reverse Transcription kit (Applied Biosystems). RT-PCR was performed in a StepOnePlus™ Real-Time PCR Systems (Applied Biosystems) with FastStart Universal SYBR Green Master Mix (Roche). ΔCt values were calculated using GAPDH as reference gene. The sequences of RT-PCR primers are as follows: GAPDH, forward primer: 5'-GTCTCCTCTGACTTCAACAGCG-3'; reverse primer, 5'-ACCACCCTGTTGCTGTAGCCAA-3'; AHR, forward primer: 5'-CTTAGGCTCAGCGTCAGTTA-3'; reverse primer, 5'-GTAAGTTCAGGCCTTCTCTG-3'; ID2, forward primer: 5'-TTGTCAGCCTGCATCACCAGAG-3';

reverse primer, 5'-AGCCACACAGTGCTTTGCTGTC-3'; NFIL3, forward primer: 5'-TGGAGAAGACGAGCAACAGGTC-3'; reverse primer, 5'-CTTGTGTGGCAAGGCAGAGGAA-3'; ZBTB16, forward primer: 5'-GAGCTTCCTGATAACGAGGCTG-3'; reverse primer, 5'-AGCCGCAAACTATCCAGGAACC-3'; TOX, forward primer: 5'-AGCATACAGAGCCAGCCTTG-3'; reverse primer, 5'-TGCATGGCAGTTAGGTGAGG-3'; and TCF1, forward primer: 5'-TGCAGCTATACCCAGGCTGG-3'; reverse primer, 5'-CCTCGACCGCCTCTTCTTC-3'.

Cell culture and differentiation assays

OP9-DL1 or OP9 stromal cells were maintained in Minimum Essential Medium α (Lonza) supplemented with 10% FCS. Flow cytometry-purified CD8a$^-$ int-ILCs or CD94$^+$CD117$^-$, CD94$^-$CD117$^-$ and CD94$^-$CD117$^+$ subpopulations (500 cells/well) or CD8a$^+$ int-ILCs (100 cells/well) were co-cultured with irradiated OP9 or OP9-DL1 stromal cells (1,500 RAD, 5,000 cells/well) in a 96 well plate (Corning) and maintained in culture medium (IMDM supplemented with 10% human serum or in culture medium containing 25 ng/mL SCF (Miltenyi Biotec), 25 ng/mL IL-7 (Peprotech), 10 U/mL IL-2 (Novartis) and 10 ng/mL IL-15 (R&D Systems) or only IL-15. The phenotype of generated progeny was determined by flow cytometry.

Cytokine secretion

CD8a$^-$ int-ILCs and ILC3 (2,000 cells/well) were stimulated with 10 U/mL IL-2 (Novartis), 50 ng/mL IL-1β (Peprotech) and 50 ng/mL IL-23 (Peprotech) for 4 days. TNF-a, IL-17A and IL-22 were measured by using Bio-Plex Pro™ human cytokine 17-plex panel kit and Bio-Plex Pro™ human Treg cytokine panel 12-plex kit (Bio-Rad).

Online supplemental material

Fig. S1 shows the mass cytometry-based analysis of the entire immune system in the human fetal intestine. Fig. S2. Top panel: t-SNE plots revealing the major lineage subsets, Bottom panel: t-SNE analysis of the innate cell compartment in the individual fetal samples. Fig. S3 shows Ki-67 and transcription factor expression profiles of fetal intestinal ILCs ex vivo. Fig. S4 is related to **Fig. 5**, and shows that CD8a$^-$ int-ILC can differentiate into CD45RA$^+$ NK Cells and ILC3. Table S1 lists the information of antibodies used in the mass cytometry data.

Author contributions

NL, VvU and FK conceived the study and wrote the manuscript. NL performed most experiments with the help of VvU. TH, NP, VvU, EE, AV and BL developed the Cytosplore application. VvU and NL performed mass cytometry analyses. AT performed the RT-PCR. SCdSL provided human fetal intestines. JvB provided conceptual input. All authors discussed the results and commented on the manuscript.

Acknowledgements

We thank the Center for Contraception, Abortion and Sexuality (CASA) in Leiden and The Hague for their efforts in collecting and providing the fetal material, K. Lodder, T. van Herwaarden, Dr. M. Bialecka, Dr. F. Wang and M. Gomes Fernandes for the dissection of the fetal intestines, E. de Haas for flow cytometric cell sorting and E. van Beelen for Luminex assay. This research was supported by the Leiden University Medical Center, The Netherlands Organization for Scientific Research (ZonMW grant 91112008) and NWO Applied Technical Sciences grant 12721 (VANPIRE). N. Li was supported by the China Scholarship Council. We thank Drs. F.J.T. Staal, K. Schepers and T. Cupedo for critical review of the manuscript.

The authors declare no competing financial interests.

References

1. Spits, H. et al. Innate lymphoid cells--a proposal for uniform nomenclature. Nat. Rev. Immunol. 13, 145–149 (2013).
2. Hazenberg, M. D. & Spits, H. Human innate lymphoid cells. Blood 124, 700–709 (2014).
3. Cella, M. et al. A human natural killer cell subset provides an innate source of IL-22 for mucosal immunity. Nature 457, 722–725 (2009).
4. Cupedo, T. et al. Human fetal lymphoid tissue-inducer cells are interleukin 17-producing precursors to RORC+ CD127+ natural killer-like cells. Nat. Immunol. 10, 66–74 (2009).
5. Gasteiger, G., Fan, X., Dikiy, S., Lee, S. Y. & Rudensky, A. Y. Tissue residency of innate lymphoid cells in lymphoid and nonlymphoid organs. Science 350, 981–985 (2015).
6. Juelke, K. & Romagnani, C. Differentiation of human innate lymphoid cells (ILCs). Curr. Opin. Immunol. 38, 75–85 (2016).
7. Ishizuka, I. E., Constantinides, M. G., Gudjonson, H. & Bendelac, A. The Innate Lymphoid Cell Precursor. Annu. Rev. Immunol. 34, 299–316 (2016).
8. Possot, C. et al. Notch signaling is necessary for adult, but not fetal, development of RORγt(+) innate lymphoid cells. Nat. Immunol. 12, 949–958 (2011).
9. Montaldo, E. et al. Human RORγt CD34 Cells Are Lineage-Specified Progenitors of Group 3 RORγt Innate Lymphoid Cells. Immunity 41, 988–1000 (2014).
10. Scoville, S. D. et al. A Progenitor Cell Expressing Transcription Factor RORγt Generates All Human Innate Lymphoid Cell Subsets. Immunity 44, 1140–1150 (2016).
11. Lim, A. I. et al. Systemic Human ILC Precursors Provide a Substrate for Tissue ILC Differentiation. Cell 168, 1086–1100.e10 (2017).
12. Bernink, J. H. et al. Human type 1 innate lymphoid cells accumulate in inflamed mucosal tissues. Nat. Immunol. 14, 221–229 (2013).
13. Bernink, J. H. et al. Interleukin-12 and -23 Control Plasticity of CD127(+) Group 1 and Group 3 Innate Lymphoid Cells in the Intestinal Lamina Propria. Immunity 43, 146–160 (2015).
14. Lim, A. I. et al. IL-12 drives functional plasticity of human group 2 innate lymphoid cells. J. Exp. Med. 213, 569–583 (2016).
15. Bal, S. M. et al. IL-1β, IL-4 and IL-12 control the fate of group 2 innate lymphoid cells in human airway inflammation in the lungs. Nat. Immunol. 17, 636–645 (2016).
16. Bandura, D. R. et al. Mass cytometry: technique for real time single cell multitarget immunoassay based on inductively coupled plasma time-of-flight mass spectrometry. Anal. Chem. 81, 6813–6822 (2009).
17. van Unen, V. et al. Visual analysis of mass cytometry data by hierarchical stochastic neighbour embedding reveals rare cell types. Nat. Commun. (2017).
18. van Unen, V. et al. Mass Cytometry of the Human Mucosal Immune System Identifies Tissue- and Disease-Associated Immune Subsets. Immunity 44, 1227–1239 (2016).
19. Maaten, L. van der & Hinton, G. Visualizing Data using t-SNE. J. Mach. Learn. Res. 9, 2579–2605 (2008).
20. Shekhar, K., Brodin, P., Davis, M. M. & Chakraborty, A. K. Automatic Classification of Cellular Expression by Nonlinear Stochastic Embedding (ACCENSE). Proc. Natl. Acad. Sci. U. S. A. 111, 202–207 (2014).
21. Höllt, T. et al. Cytosplore: Interactive Immune Cell Phenotyping for Large Single-Cell Datasets. Comput. Graph. Forum 35, 171–180 (2016).
22. Björklund, Å. K. et al. The heterogeneity of human CD127(+) innate lymphoid cells revealed by single-cell RNA sequencing. Nat. Immunol. 17, 451–460 (2016).
23. Simoni, Y. et al. Human Innate Lymphoid Cell Subsets Possess Tissue-Type Based Heterogeneity in Phenotype and Frequency. Immunity 46, 148–161 (2017).
24. Bendall, S. C. et al. Single-Cell Trajectory Detection Uncovers Progression and Regulatory Coordination in Human B Cell Development. Cell 157, 714–725 (2014).

25. Artis, D. & Spits, H. The biology of innate lymphoid cells. Nature 517, 293–301 (2015).

26. Freud, A. G. et al. Evidence for discrete stages of human natural killer cell differentiation in vivo. J. Exp. Med. 203, 1033–1043 (2006).

27. Klose, C. S. N. et al. Differentiation of type 1 ILCs from a common progenitor to all helper-like innate lymphoid cell lineages. Cell 157, 340–356 (2014).

28. Setty, M. et al. Wishbone identifies bifurcating developmental trajectories from single-cell data. Nat. Biotechnol. 34, 637–645 (2016).

29. Pezzotti, N. et al. Approximated and User Steerable tSNE for Progressive Visual Analytics. IEEE Trans. Vis. Comput. Graph. (2016). doi:10.1109/TVCG.2016.2570755

30. Mjösberg, J. M. et al. Human IL-25- and IL-33-responsive type 2 innate lymphoid cells are defined by expression of CRTH2 and CD161. Nat. Immunol. 12, 1055–1062 (2011).

31. Yang, Q. et al. TCF-1 upregulation identifies early innate lymphoid progenitors in the bone marrow. Nat. Immunol. 16, 1044–1050 (2015).

32. Ishizuka, I. E. et al. Single-cell analysis defines the divergence between the innate lymphoid cell lineage and lymphoid tissue-inducer cell lineage. Nat. Immunol. 17, 269–276 (2016).

33. Bando, J. K., Liang, H.-E. & Locksley, R. M. Identification and distribution of developing innate lymphoid cells in the fetal mouse intestine. Nat. Immunol. 16, 153–160 (2015).

34. Renoux, V. M. et al. Identification of a Human Natural Killer Cell Lineage-Restricted Progenitor in Fetal and Adult Tissues. Immunity 43, 394–407 (2015).

35. Satoh-Takayama, N. et al. IL-7 and IL-15 independently program the differentiation of intestinal CD3-NKp46+ cell subsets from Id2-dependent precursors. J. Exp. Med. 207, 273–280 (2010).

36. Kotecha, N., Krutzik, P. O. & Irish, J. M. Web-based analysis and publication of flow cytometry experiments. Curr. Protoc. Cytom. Chapter 10, Unit10.17 (2010).

Supplemental information

	Antigen	Tag	Clone	Supplier	Cat.	Final dilution
1	CD127	^{165}Ho	AO19D5	DVS	3165008B	1/800
2	CCR6	^{141}Pr	G034E3	DVS	3141003A	1/200
3	CD8a	^{146}Nd	RPA-T8	DVS	3146001B	1/200
4	CD11c	^{162}Dy	Bu15	DVS	3162005B	1/200
5	CD38	^{172}Yb	HIT2	DVS	3172007B	1/200
6	CD45	^{89}Y	HI30	DVS	3089003B	1/100
7	CD117	^{143}Nd	104D2	DVS	3143001B	1/100
8	CD4	^{145}Nd	RPA-T4	DVS	3145001B	1/100
9	CD16	^{148}Nd	3G8	DVS	3148004B	1/100
10	CD25	^{149}Sm	2A3	DVS	3149010B	1/100
11	CD123	^{151}Eu	6H6	DVS	3151001B	1/100
12	CD7	^{153}Eu	CD7-6B7	DVS	3153014B	1/100
13	CD163	^{154}Sm	GHI/61	DVS	3154007B	1/100
14	CCR7	^{159}Tb	G043H7	DVS	3159003A	1/100
15	CD14	^{160}Gd	M5E2	DVS	3160001B	1/100
16	CD161	^{164}Dy	HP-3G10	DVS	3164009B	1/100
17	CD27	^{167}Er	O323	DVS	3167002B	1/100
18	CD45RA	^{169}Tm	HI100	DVS	3169008B	1/100
19	CD3	^{170}Er	UCHT1	DVS	3170001B	1/100
20	PD-1	^{175}Lu	EH 12.2H7	DVS	3175008B	1/100
21	CD56	^{176}Yb	NCAM16.2	DVS	3176008B	1/100
22	CD11b	^{144}Nd	ICRF44	DVS	3144001B	1/100
23	TCRgd	^{152}Sm	11F2	DVS	3152008B	1/50
24	HLA-DR	^{168}Er	L243	BioL	307651	1/200
25	CD20	^{163}Dy	2H7	BioL	302343	1/200
26	CD34	^{142}Nd	HIB19	BioL	343531	1/100
27	IgM	^{150}Nd	MHM88	BioL	314527	1/100
28	CD103	^{155}Gd	Ber-ACT8	BioL	350202	1/100
29	CRTH2	^{156}Gd	BM16	BioL	350102	1/100
30	CD28	^{171}Yb	CD28.2	BioL	302902	1/100
31	CD45RO	^{173}Yb	UCHL1	BioL	304239	1/100
32	CD122	^{158}Gd	TU27	BioL	339002	1/50
33	KLRG-1	^{161}Dy	REA261	MACS	120-014-229	1/50
34	CD8b	^{166}Er	SIDI8BEE	ebio	14-5273	1/50
35	NKp46	^{174}Yb	9E2	BioL	331902	1/40
DVS Sciences (DVS), eBioscience (eBio) and Biolegend (BioL).						

Table S1. CyTOF antibody panel
The conjugation, validation and titration of all the antibodies which were not bought from DVS were done in house.

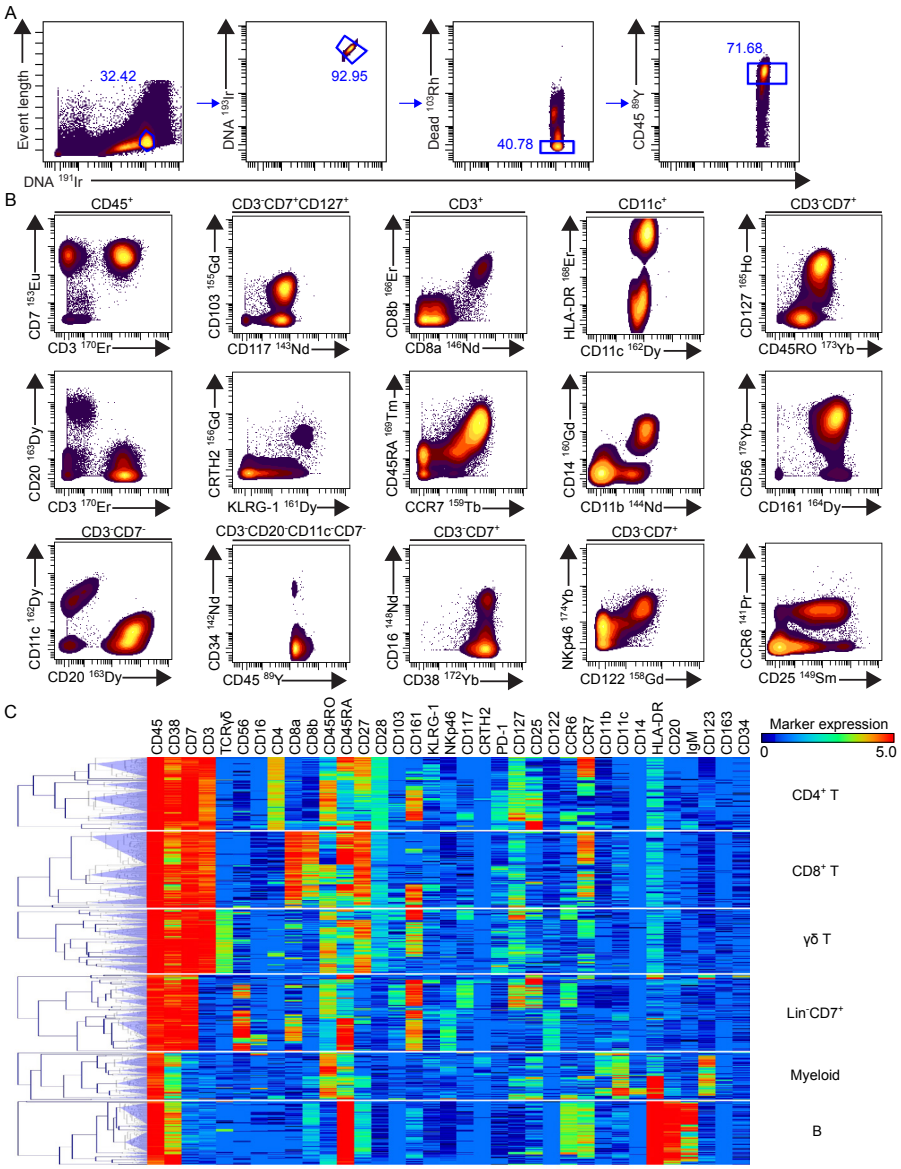

Fig. S1. Analysis of the entire immune system in the human fetal intestine using mass cytometry. (**A**) Representative biaxial density dot plots from one fetal intestine showing the gating strategy for single, live CD45+ cells with percentages analysed by mass cytometry (N=7). Event length is a mass cytometry parameter defined as signal duration for the number of scans taken to acquire a given ion cloud. (**B**) Representative biaxial density dot plots from one fetal intestine showing the typical cell staining profiles of the antibodies used in mass cytometry after gating as shown in panel A (N=7). Gated cell populations are annotated above the plots. (**C**) A heatmap showing the median ArcSinh5-transformed marker expression values of the total 907 clusters identified by analyzing the entire immune system ($CD45^+$ cells) from 7 fetal intestines using the t-SNE-ACCENSE analysis pipeline (clustering per individual sample) for each of the 6 major immune lineages individually, as described before[18], and hierarchical clustering thereof. four independent experiments).

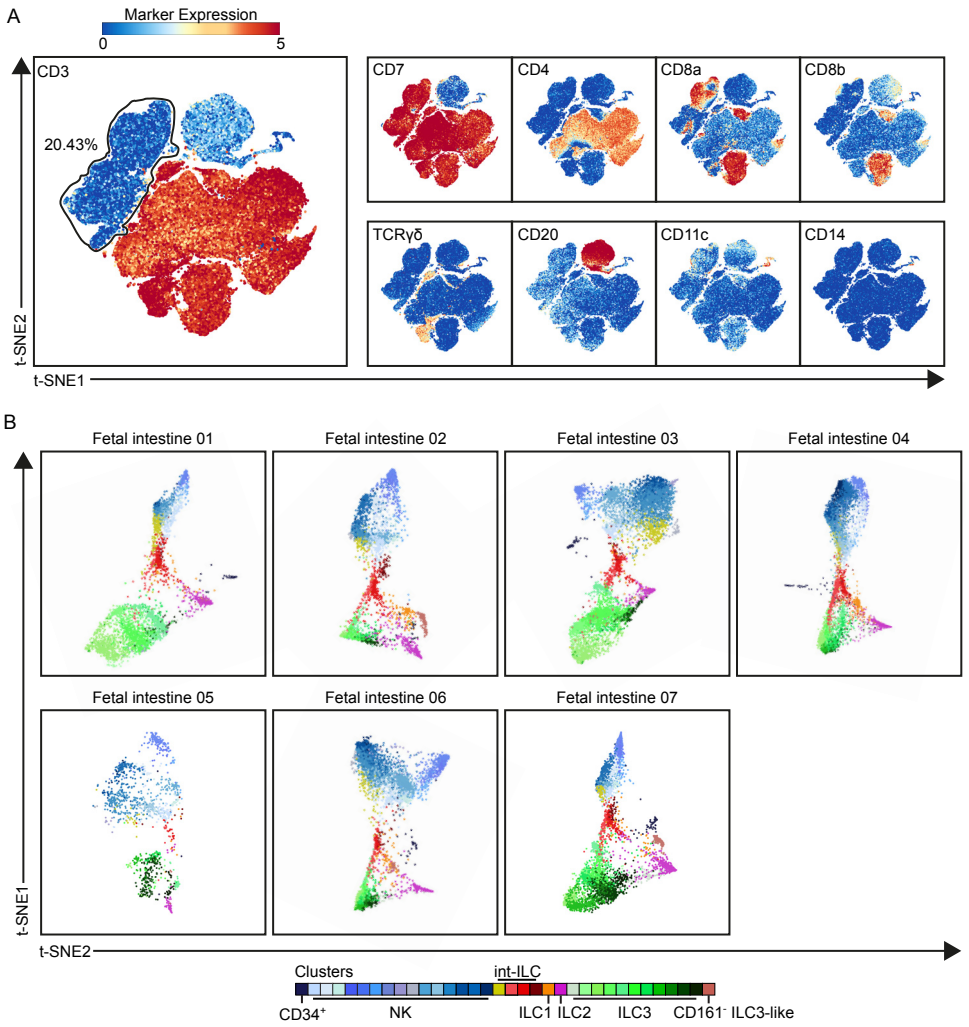

Fig. S2. t-SNE-based analysis of the Lin$^-$CD7$^+$ innate immune compartment in the human fetal intestine. (A) Gating strategy of the Lin$^-$CD7$^+$ innate cell population in the human fetal intestine. t-SNE embeddings of the collective CD45$^+$ cells (2.2x10^5 cells) from 7 fetal intestines at single-cell resolution. Colors of cells represent ArcSinh5-transformed expression values of indicated markers. (**B**) Monitoring t-SNE computation dynamics for each individual fetal intestine. t-SNE embeddings of the ILC mass cytometry data showing single cells at stage 4 of the optimization course of the t-SNE computation for each individual fetal intestine (N=7). Colors represent the cluster partitions.

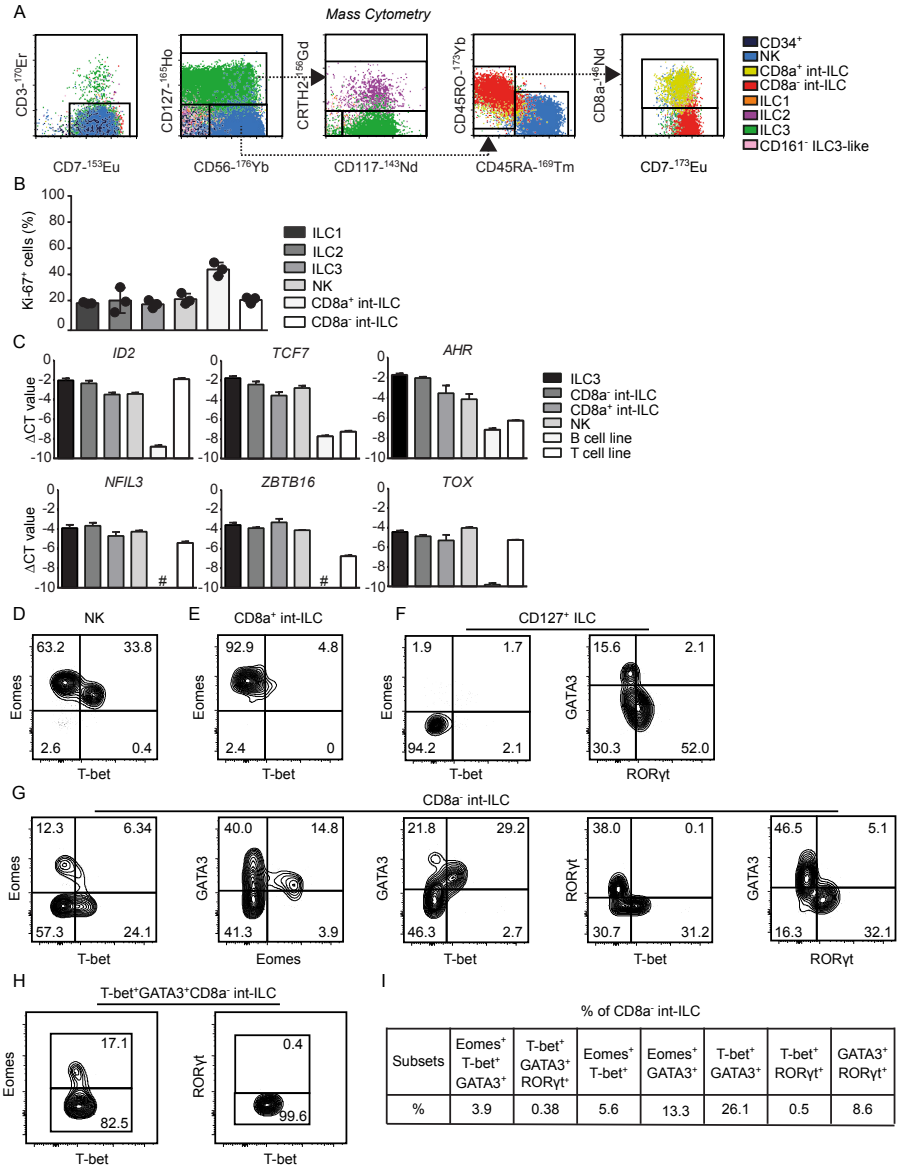

Subsets	Eomes+ T-bet+ GATA3+	T-bet+ GATA3+ RORγt+	Eomes+ T-bet+	Eomes+ GATA3+	T-bet+ GATA3+	T-bet+ RORγt+	GATA3+ RORγt+
%	3.9	0.38	5.6	13.3	26.1	0.5	8.6

Fig. S3. Ki-67 and transcription factor expression profiles of fetal intestinal ILCs *ex vivo*. (**A**) Minimal antibody panel required for phenotyping ILC and int-ILC subsets in the human fetal intestine. Biaxial plots showing the expression of the indicated markers by ILC1, ILC2, ILC3, NK and int-ILC subsets based on mass cytometry data derived from 7 human fetal intestines. Color represents the different subsets identified by the t-SNE-based analysis shown in Fig. 1 B and numbers of x-axis and y-axis represent ArcSinh5-transformed expression values of indicated markers. (**B**) Quantification of Ki-67 positive cells within indicated subsets obtained from 3 different human fetal intestines (Two independent experiments). Error bar shows mean ± SD. (**C**) Relative mRNA expression of ID2, TCF, AHR, NFIL3, ZBTB16 and TOX by the purified ILC subsets, B and T cell lines analyzed by RT-PCR (Three independent experiments). GAPDH as reference gene. # indicates that the ΔCt value is below -10. Error bar shows mean ± SD. (**D**) Representative biaxial plots showing the expression of T-bet and Eomes, and GATA3 and RORγt by fetal intestinal CD127$^+$ ILC. (**E-F**) Representative biaxial plots showing the expression of T-bet and Eomes by (**E**) fetal intestinal NK cells, and (**F**) CD8a$^+$ int-ILC as defined in Fig. 3 A with flow cytometry. (**G**) Representative biaxial plots showing the combinatorial expression profiles of Eomes, T-bet, GATA3 and RORγt by fetal intestinal CD8a$^-$ int-ILC. (**H**) Expression of Eomes and RORγt by fetal intestinal T-bet$^+$GATA3$^+$CD8a$^-$ int-ILC. (**I**) Quantification of transcription factor positive cells of fetal intestinal CD8a$^-$ int-ILC. (Two independent experiments).

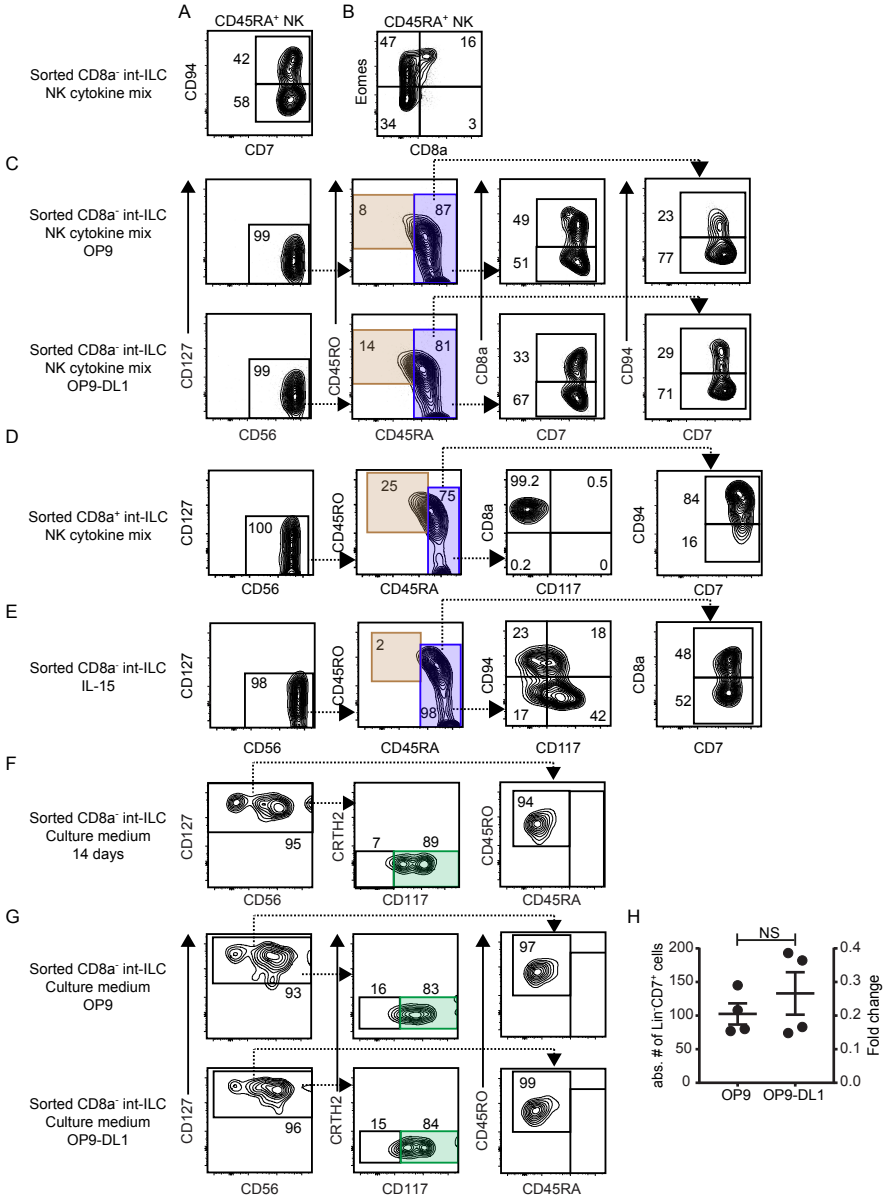

Fig. S4. CD8a⁻ int-ILC can differentiate into CD45RA⁺ NK Cells and ILC3. (**A-E**) Purified CD8a⁻ int-ILC (500 cells/well) and CD8a⁺ int-ILC (100 cells/well) populations were co-cultured with irradiated OP9-DL1 or OP9 stromal cells for 7 days either with culture medium supplemented with SCF, IL-7, IL-2, IL-15 (referred to as NK cytokine mix) or supplemented with IL-15. Generated cells were harvested and analyzed by flow cytometry. Duplicated wells were included for each condition in each experiment. Representative plots show a single duplicate. (**A and B**) Biaxial plots show the expression of CD94 (**A**) and the transcription factor Eomes (**B**) by generated CD45RA⁺ NK cells from sorted CD8a- int-ILCs with NK cytokine mix. (Three to five independent experiments). (**C-E**) Representative biaxial plots depict the phenotypes of the generated Lin⁻CD7⁺ cells from (**C**) sorted CD8a⁻ int-ILCs with NK cytokine mix with irradiated OP9-DL1 or OP9 stromal cells and (**D**) sorted CD8a⁺ int-ILCs with NK cytokine mix and (**E**) sorted CD8a⁻ int-ILCs with IL-15. (Two independent experiments). (**F-H**) Purified CD8a⁻ int-ILC (500 cells/well) were co-cultured either with irradiated OP9-DL1 or with OP9 stromal cells with cytokine-free culture medium for 14 days (**F**) and 7 days (**G and H**). Generated cells were harvested and analyzed by flow cytometry (**F and G**). Representative biaxial plots depict the phenotypes of the generated Lin⁻CD7⁺ cells. (Two independent experiments). (**H**) Quantification in absolute cell number (left axis) and fold change (right axis) compared to the number of initially sorted cells. (Two independent experiments). Error bar shows mean ± SEM.